fluids

MDPI

Article

Aerofoil Flow Sensing Using On-Board Optical Tracking of Flexible Pillar Sensors

Omar Selim * and Christoph Brücker

Department of Engineering, City, University of London, Northampton Square, London EC1V 0HB, UK; christoph.bruecker@city.ac.uk
* Correspondence: omar.selim@city.ac.uk

Abstract: A novel approach for sensing and characterising the flow over an aerofoil is introduced. Arrays of flexible wind-hair-like sensors distributed over an aerofoil, which are tracked remotely using high-speed imaging and processing, acting as "digital tufts", are used to provide real-time readings of local flow information with high temporal resolution. The use case presented in this paper has the sensors embedded within the suction side of a NACA0012 aerofoil and tested in a wind tunnel for varying angles of attack in static and dynamic tests. The time-averaged signals were able to provide information pertaining to the free-stream velocity and instantaneous angle of attack. The capability of the sensor type to provide temporal flow information is also explored. The sensors were used to detect low-frequency oscillations, which are pre-cursory to stall. These are hypothesised to be linked to breathing modes of the laminar separation bubble, causing a shear-layer flapping observed on the sensors. Such low-frequency oscillations were also detected shortly before separation in the ramp-up studies.

Keywords: aerodynamics; sensor; nature inspired

Citation: Selim, O.; Brücker, C. Aerofoil Flow Sensing Using On-Board Optical Tracking of Flexible Pillar Sensors. *Fluids* **2023**, *8*, 146. https://doi.org/10.3390/fluids8050146

Academic Editor: D. Andrew S. Rees

Received: 10 April 2023
Revised: 26 April 2023
Accepted: 27 April 2023
Published: 30 April 2023

1. Introduction

With the introduction of small and medium UAVs into everyday commercial and non-commercial operations, the importance of accurate, reliable, and robust sensing systems has become more and more apparent. This is especially true in the case of AI-powered autonomous flight, where machine learning algorithms are employed to make critical decisions without human intervention. Various strategies for safe and effective autonomous flight control exist for navigation [1,2], which rely on a number of sensing and inertial systems. However, with the increase in the scale of such operations, it is important that flight is also optimised for efficiency.

The primary difference between conventional flight control strategies in both manned and unmanned fixed-wing flight, in contrast to the flight control seen in natural fliers such as birds and insects, is the sensing distribution and redundancy. Rather than the conventional reliance on single point-mass calculations, coupled with a finite number of reduced pressure readings from selected points over the aircraft body, it is seen that natural fliers will rely on a plethora of distributed sensors around the body, providing a real-time picture of flow phenomena that can be correlated to specific flight conditions. Investigations of biologically inspired sensors have shown a variety of natural fliers using wing receptors to detect temporal flow and pressure changes, in addition to variations in amplitude for signals of the same frequency for executive decision making in flight control and stabilisation [3]. This is important when considering the high flexibility of such natural fliers in comparison to the relatively rigid airframes of current aircraft and their associated complex flight dynamics models [4]. Even in high-speed flight, mechanoreceptors on fast fliers have the ability to scale with flow conditions to a high level of sensitivity [5], which is critical during high-speed stoops where small changes to angle of attack (AoA) can have significant effects on lift generation and flight stability [6].

Inspired from nature, wind-hair receptors were explored in [7] to detect changes in the boundary layer velocity profiles, giving detailed information of the overall flow conditions. When those sensors are exposed to flow, they show a deflection response as a result of the length-integrated load distribution along the filamentous hairs. Their response was tested under the different shape factors of the velocity profile and for different boundary layer thicknesses, and the researchers concluded that such wind-hairs are sensitive to flow profile changes from favourable to adverse pressure gradients. Micro-pillar shear stress sensors are even able to directly sense the velocity gradient at the wall [8] and, as such, can be used to detect local flow reversals [9]. Their mechanical behavior is well defined under static and dynamic load conditions; therefore, the sensors can quantify the wall-shear stress in magnitude and direction. This, however, limits the size of those sensors in practical applications to the scale of the viscous boundary layer, which is typically in the sub-millimeter range. For practical application, larger "wind-hairs" could be a compromise between gain in sensitivity (stronger bending forces) and the loss of spatial resolution that occurs due to the wall-normal integration effect.

This paper will introduce work carried out on elastic bio-inspired wind-hairs in the form of flexible cantilever structures used for aerofoil flow sensing on an NACA0012 model. Moreover, the novel incorporation of remote optical tracking of such pillars is discussed using a combination of physical wavelength separation, on-board high-speed photography, and a cross-correlation algorithm to obtain a real-time output from such sensors while mitigating the requirement of a physical connection. It is not guaranteed that a physical connection between a sensor and computer on-board a compact UAV will always be available, especially with the emergence of materials of higher strength-to-weight ratios and with modern manufacturing techniques allowing the creation of more complex designs optimised for efficiency rather than internal space. Thus, such remote optical monitoring of sensors allows the capability to obtain flow measurements from areas that otherwise would remain unreachable with traditional point-pressure measurements to provide an AI flight controller with a more complete flow picture for decision making.

The design, fabrication, characterisation, and calibration of the sensor system is discussed, in addition to in situ calibration and FEA simulations that were carried out to characterise the sensor response in air. Furthermore, several use cases for such sensors are presented in a series of wind-tunnel experiments simulating the flight conditions and system response when placed in a single-row array over the suction side of an aerofoil. Mounting the sensors on an NACA0012 foil was chosen as a use case to explore the sensor's response to varying conditions at low Reynolds numbers. The flow over an NACA0012 at such Reynolds numbers is well known from the literature [10–12] and is within the range for conditions faced by most small- and medium-scale UAVs.

Firstly, sensitivity to the growth of the boundary layer over the suction side of the aerofoil and its relationship to changes in AoA are explored, and the time-averaged response to such conditions is obtained and compared. Furthermore, characteristic fluctuations of the velocity profile that correlate to flow phenomena unique to those AoAs that are incipient to flow separation are detected. Such correlations are known to exist from previous CFD simulations and TR-PIV measurements on an NACA0012 aerofoil undergoing stall [13–15], where it was seen that the frequency of the low-frequency oscillations increased with AoA at the onset of stall.

2. Materials and Methods

2.1. Aerofoil Preparation

The design and manufacturing of the pillar sensors follows the concept previously discussed in [16], which follows the methodology described in earlier work [17] using flexible micro-pillars to detect and characterise wall shear stress in the aortic artery. The sensors were scaled up to match the scale and application of the current investigation to act as 'digital tufts' over the wing surface.

The aerofoil model used was a constant NACA0012 aerofoil with a chord length of 0.19 m and a span of 0.70 m. It was assembled from segments of 3D-printed NACA-0012 sections with a Perspex centre section to provide optical access through the mid-span location (Figure 1). These sections were clamped together with the sheet of pillars placed in between at one side of the transparent segment. The sheet was made from a silicone film (see Table 1), which was the base of the pillars and was laser-cut to the outer contour of the aerofoil. At the outer edge, arrays of pillars in the shape of rectangular beams were left out (height 7.2 mm, width 0.37 mm). This method of manufacture allows for the chord-wise position variation of the pillars with minimal disruption to the experimental setup. The current pillar spacing was 15% of the chord length, with the foremost pillar lying at $0.15x/c$, and the aft-most pillar lying at $0.9x/c$, as illustrated in (Figure 1).

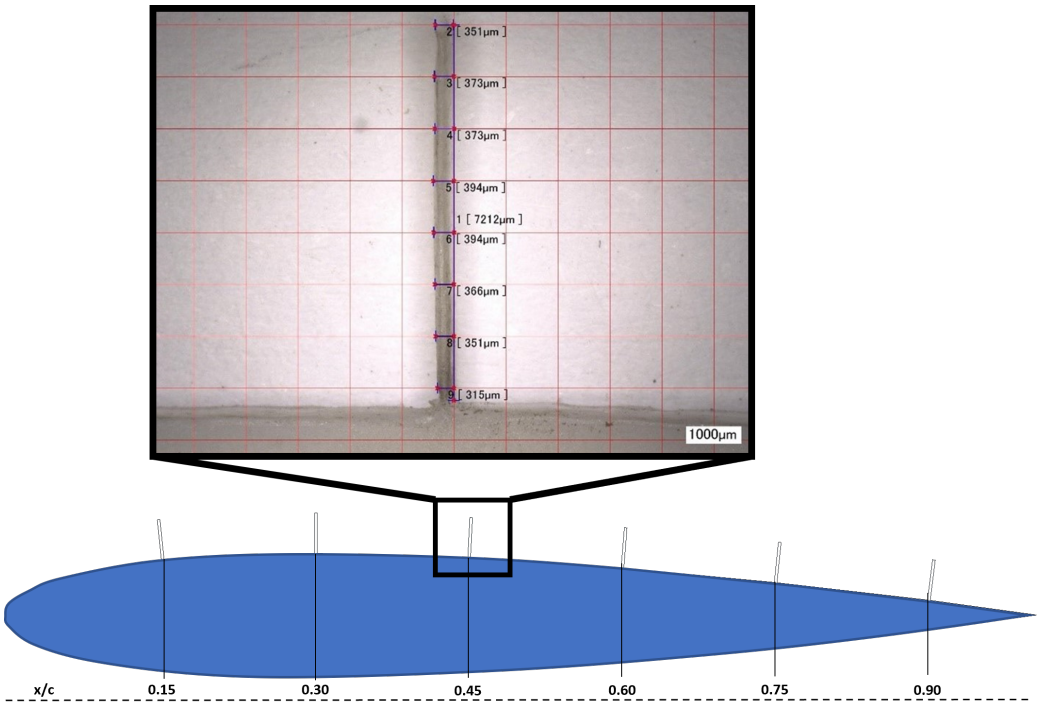

Figure 1. Magnified image of one of the pillar sensors under a 200× microscope lens showing the details of the structure and pertinent dimensions. The pillars are numbered in the following from no.1 at the uppermost left pillar to 6 at the most downstream pillar near the trailing edge. See also [16].

Table 1. Material properties for silicone rubber film.

Thickness [t]	**Density** [ρ]	**Young's Modulus** [E]
2 mm	1.2 g/cm^3	2.45 MPa

Furthermore, the rectangular cross-section leverages the second moment of area in favour of chord-wise deflections rather than span-wise deflections. For the use case discussed herein, chord-wise velocity perturbations are of greater importance, and span-wise perturbations are naturally eliminated due to the higher second moment of area about that axis. When the sheet is clamped between the 3D-printed section and the perspex section, it is flush with the surface, while the pillars protrude into the flow at a right angle to the local surface (Figure 2). The pillar tips and specific marker points along the chord are labelled with florescent dye (MMA-RhB-Frak-Paticles, Dantec Dynamics, with a peak emission at 584 nm and a peak absorption at 540 nm) and illuminated with an LED illuminator (IL-105/6X Illuminator, HardSoft, Obergriesbach, Germany). Thus, using optical lens filters for the wavelength separation of the emitted light, the images of the tips can be isolated from the surrounding background.

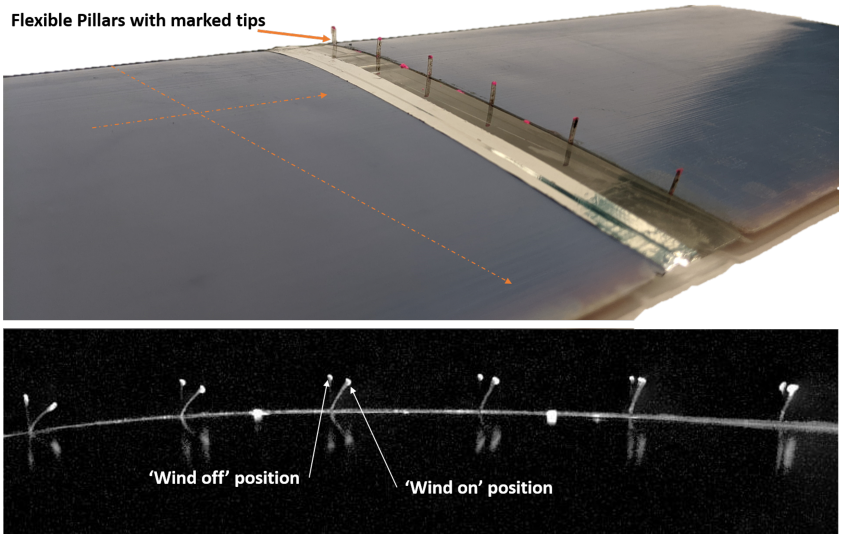

Figure 2. (**Top**) Image from 'wing-root' position showing the different components of the model; in blue are the 3D-printed aerofoil sections, and between is a transparent Perspex section, also showing the flexible pillars emanating from the surface, which could be extended to a full 'skin' with 2D arrays of sensors. (**Bottom**) Overlaid images from the object tracking camera in the simulated 'on-board' position showing sample pillar deflections (flow is left to right). See also [16].

2.2. Wind Tunnel Setup

The model was placed in the T2 tunnel of the Handley–Page lab at City, University of London. This is a closed-loop wind tunnel with a turbulence intensity of 0.8 %. The test section was 0.81 m $\times$ 1.22 m, where the model was mounted such that one end of the aerofoil spans to the floor, while the free end is fitted with an end-plate to negate tip effects. Optical access was achieved through one transparent side window and the bottom, which was used to illuminate the sensor tips and record their tip-motion. Supportive flow measurements were made with a time-resolved PIV system, which was arranged with the light sheet in the plane of the pillars. The experimental setup for the PIV system can be seen in (Figure 3). A Phantom M310 camera was arranged orthogonally to the laser sheet and fitted with an 100 mm lens. A Litron LDY300 dual-head laser was used to illuminate the measurement plane. Seeding was carried out using DEHS tracer particles injected into the flow in the settling chamber upstream of the wind tunnel nozzle. Insight V3V-4G software was used to coordinate the laser pulses and image capture at a repetition rate of 1 kHz and a laser pulse separation of 30 µs. A standard multi-pass cross-correlation algorithm was applied with Gaussian sub-pixel accuracy and with a typical uncertainty of 0.03∼0.05 px [18], which correlates to a velocity uncertainty on the order of 0.1 m/s. The field-of-view magnification factor was 0.09, and interrogation windows of 64 $\times$ 64 px (approx. 4.35 $\times$ 4.35 mm) were applied for the first pass, halving over the following two passes, to process the image pairs and analyse the flow field.

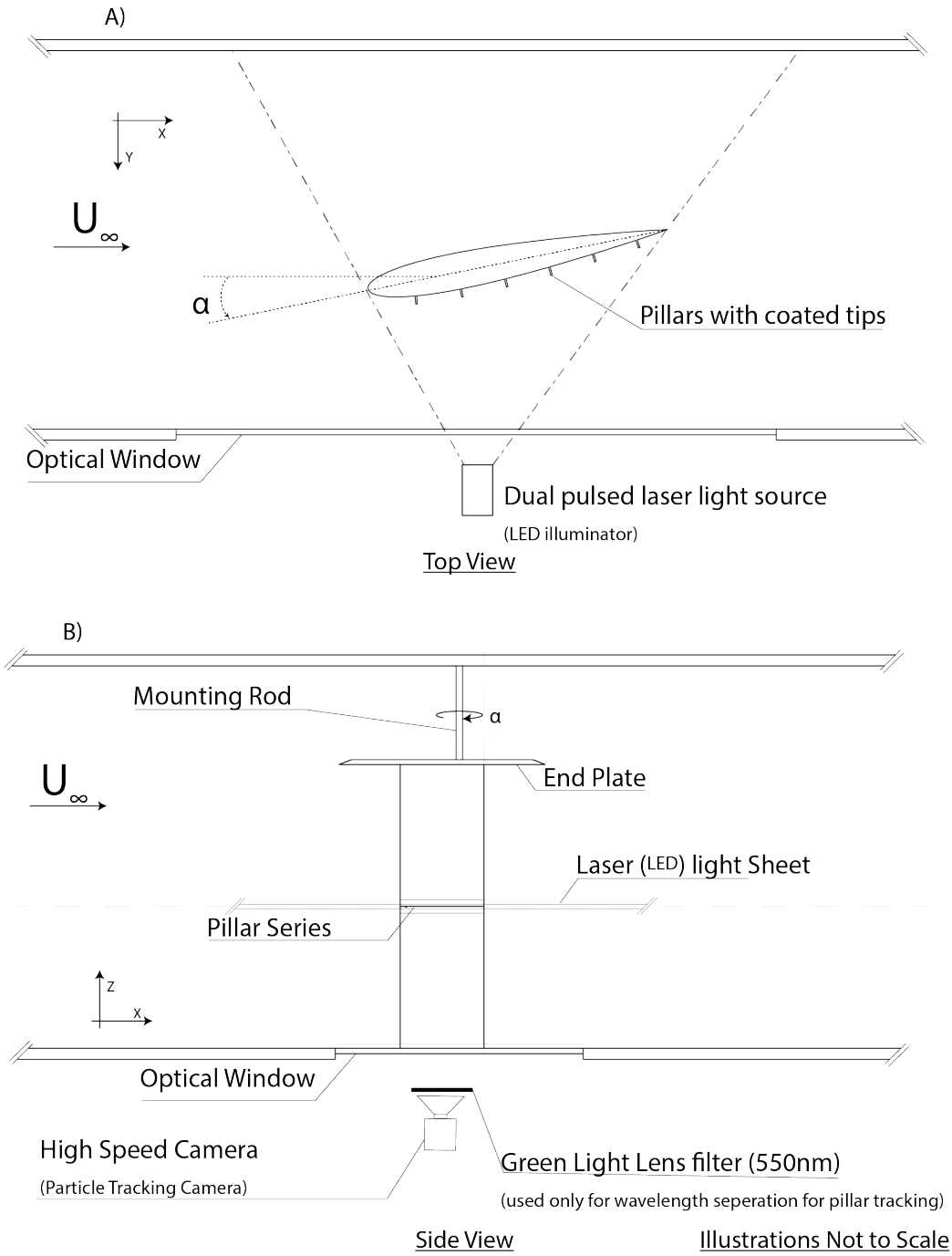

Figure 3. Experimental arrangement for the wind-tunnel studies. LED light source and laser illumination were interchangeable with minimal disruption. Text between brackets indicates the alternative arrangement for the different experiments. (**A**) top view, (**B**) side view.

2.3. Optical Sensor Tracking

The signal detection process was the optical tracking of the sensor tip displacement Q(t), which was proportional to the bending moment imposed by the flow-induced drag forces. This was measured by comparing the location of the tip in wind-on and wind-off situations. A high-speed camera (ProcImage 500-Eagle high-speed camera, 1280 px × 1024 px, Photon Lines Ltd, Bloxham, UK) was mounted outside the tunnel along the span-wise line of the wing to simulate where an on-board camera would be mounted, and it was fitted with a green light lens filter (long-pass optical filter, cut-off wavelength of 550 nm, Edmund Optics), thus only receiving the light emission from the fluorescently labelled pillar tips

(and marker points). From this position, the camera captured the pillar tip positions at a sampling rate of 500 Hz in two different modes: standard mode, as seen in (Figure 2), fitted with a 50 mm lens, and binary mode, with the detection of the centroids of white connected pixels in a selected area in the frame. This then outputs a stream of coordinate points with a time marker corresponding to 6 pillar tips and 2 marker points. Using a 100 mm lens, a finer resolution can be obtained over 3 pillars of interest to allow more spatial resolution recordings. This method of data acquisition was also used to acquire position data for underwater artificial seal whiskers [19]. Such an object tracking camera can provide a quasi-on-line response of the flow state around the aerofoil by tracking the sensors. Additionally, using a Phantom M310, the same recordings were captured, and the positions of those tips were then found using a MATLAB-based code similar to PIV, where a small interrogation window around the tip was cross-correlated between images of wind-on and wind-off situations. This serves the purpose of validating the results from the tracking, and it also serves as a proof of concept for further work assembling pillars with an on-board camera in situ on an airborne UAV.

2.4. Sensor Calibration

In order to characterise the static and dynamic response of the pillars, mechanical tests and FEA simulations were carried out and compared. From a mechanical point of view, the pillars act as one-sided clamped cantilevered beams of nearly uniform rectangular cross-section (see Figure 1). The static deflection of the sensors was tested when exposed to a wall-jet-like flow with approximately constant velocity over the pillar length, as measured by a hot-wire probe. Subsequent finite element simulations were carried out to analyse the sensitivity of the pillar tip deflection to these variations in loading. Measurement data for a cylinder within the experimental range of Reynolds numbers [20] were used to create a power–fit approximation similar to the methods from [7,17], resulting in the drag coefficient being given in the form of Equation (1) with ($R^2 = 0.967$):

$$C_d = 3.0244 \times Re^{-0.155} \tag{1}$$

The calibration flow was generated with a small open-ended wind tunnel with a one-sided contraction nozzle at the exit (length, 75 cm; nozzle width, W = 12 cm; nozzle height, H = 10 mm; contraction ratio, 10:1) fashioned at the facilities in order to carry out the in situ calibration of the pillar sensors at the most upstream pillar near the leading edge; see (Figure 4). The flow was driven by a set of four fans at the inlet of the tunnel and exited the nozzle with the bottom wall flush aligned tangential to the upper section of the suction side, thus producing a near-constant velocity along the pillar. Flow velocities at the pillar locations were measured with a hotwire anemometer. The results show little variation of velocity over the length of the pillar; thus, for the FEA simulation, the velocity along the pillar is assumed to be constant in its first approximation.

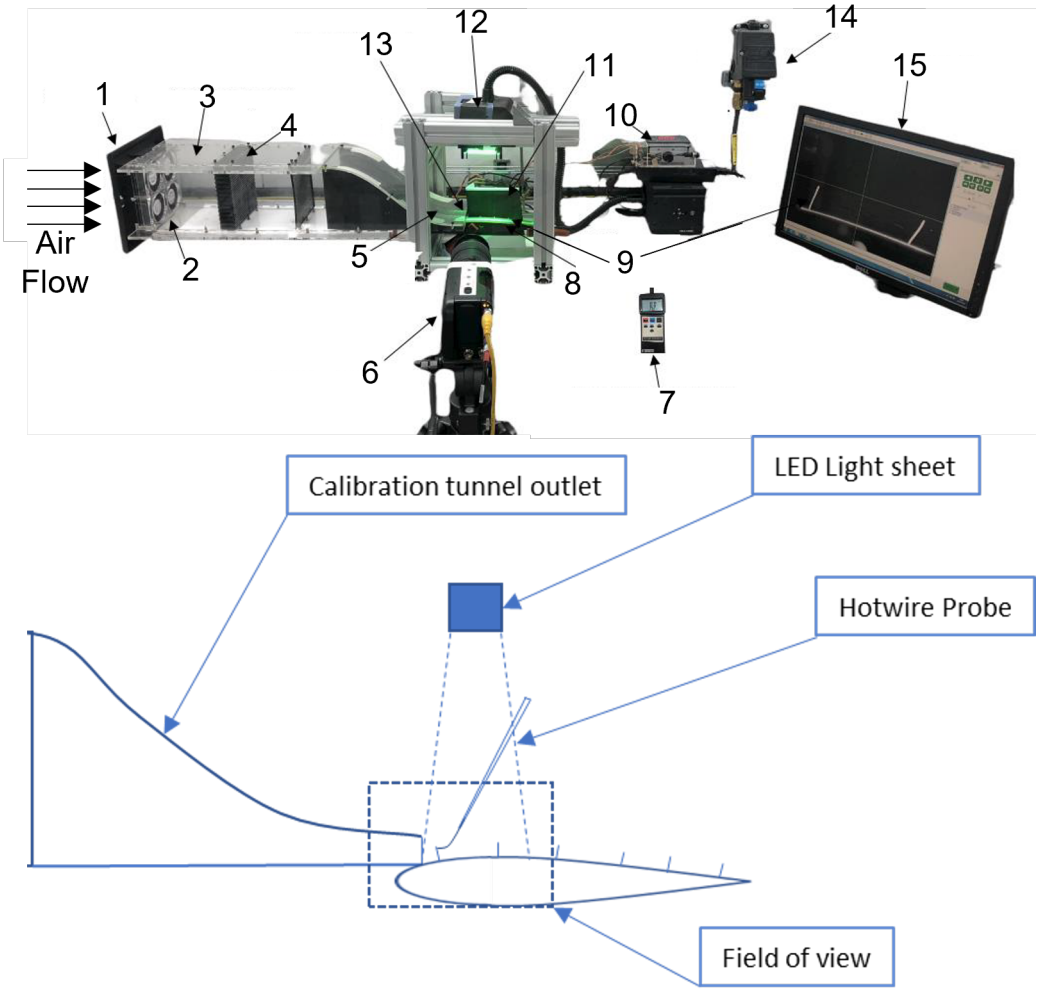

Figure 4. Experimental setup of the wall jet for sensor calibration, showing different components for various calibration-related tests. The numbered parts are as follows: 1. inlet nozzle; 2. fans (flow generator); 3. particle injection; 4. honeycomb; 5. outlet nozzle; 6. high-speed camera; 7. hot-wire anemometer; 8. aerofoil model; 9. pillar sensors; 10. speed controller; 11. background black sheet; 12. LED light; 13. hot-wire probe; 14. power supply; 15. computer.

3. Results

3.1. Calibration

The results from the calibration of the leading pillar no.1 are most significant to obtain an understanding of free-stream velocity. This pillar is located at 15% chord—thus experiencing the least effects of boundary layer thickness which, at its largest, is approximately 10% of the entire pillar length. In addition, as illustrated in Equation (3), the contribution of changes in flow velocity to the total moment in equilibrium with the elastic restoring force is a function of l, the distance along the pillar from the base. Thus, contributions from the reduction in velocity in the near-wall flow, where l is very small, are negligible. In the following, we consider Q as only the tangential component in the sensor plane (parallel to the wall), and where a subscript is applied (e.g., Q_1), this denotes the number of the pillar from 1 to 6, as indicated in the experimental setup. The mean tip deflection of the leading-most pillar $\overline{Q_1}$, which is dictated by the moment balance about the clamped end of the beam $M(t)$ defined in Equation (3), can therefore provide a reliable source of information on free-stream velocity. The effects of AoA on the deflection of the first pillar in comparison to subsequent downstream pillars are investigated further later in this section.

The instantaneous load distribution $g(t,l)$ acting normal to the longitudinal axis of the pillar is derived in analogy to work from [17], where l is the distance along the pillar normal to the surface and b is the lateral dimension of the pillar:

$$g(t,l) = q(l,t) \times b \times C_d(Re_l) \tag{2}$$

$$M(t) = \int_0^l g(t,l) \times l \, dl \tag{3}$$

The results from the experimental calibration of the leading-edge pillar are shown in (Figure 5) and labeled as "Experiment". The velocity is the tip velocity as measured by the hot-wire probe from the calibration experiment. A good agreement is found with the FEA simulation for the load distributions corresponding to the same velocities within the experiment. Two FEA studies were carried out on ANSYS on a model created from a single-pillar structure: a static structural simulation to validate the available experimental data and approximate the response outside the experimental range, and a modal analysis to study the dynamic properties of the structure. The creation of the model was guided by microscopic images of the pillar structure and with material properties matching that of the manufactured pillars. Due to the simplicity of the model, a standard 100-element mesh was generated, and to simulate the conditions, the model was clamped at the base in a cantilever setup. For the static simulations, a varying load on the projected face of the pillar in the flow direction was applied according to Equation (3). The modal analysis considered bending and torsional modes only in-plane to calculate the flutter criteria. Because of growing instabilities from the outer shear layer of the wall jet, reliable steady flows with constant velocities at the pillar could only be achieved up to free-stream velocities of 10 m/s. This is where the simulations help to extend the calibration curve to higher velocities, such as those expected in the experiments at the largest Re-numbers. The reconfiguration of the pillars is defined as the natural tendency of a flexible structure to deform with the fluid flow, hence modulating the drag experienced; as the tip deflects beyond 30% of a flexible beam's length L, the reconfiguration of the pillar is considered large [21]. The effect of reconfiguration can be seen in (Figure 5), where an increase in velocity results in less of an increase in deflection at velocities higher than approx. 12 m/s, above which the Cauchy number, as defined in [21], is larger than unity.

Moreover, the dynamic response of the sensors was obtained from a step-response test in situ, where the optical setup was the same as the wind tunnel experiments but with no flow. The pillars were deflected to an initial position and then released, leading to a damped oscillatory motion back to the resting position, as plotted in (Figure 6). The natural frequency is estimated from the plot to be approximately 59 Hz, which is in good agreement with the FEA simulation (Figure 7) of the first bending mode (corresponding to the natural frequency in a vacuum situation with no damping). Higher-order bending and torsional twists are also estimated from the simulations and occur only at about 7–8 times higher frequencies, which are not of relevance for the current moderate Re-number flows. Similarly, flutter only happens at excitation frequencies higher than 230 Hz, as calculated according to [22].

With the given data of the static and dynamic responses, the postprocessing of the data was tailored to recover only the low-frequency content of the pillar motion using a low-pass filter with a cut-off frequency of 20 Hz. This ensures, on one hand, high enough temporal resolution for the expected low-frequency oscillations related to incipient stall, while it removes noise from self-excited vibrations or small-scale turbulent structures. Additionally, the range of free-stream velocities tested herein is below those that would send the pillars into flutter. Higher Reynolds number flows correspond with larger reconfigurations, which also means that the effects of vortex-induced vibrations on the pillar are limited [23].

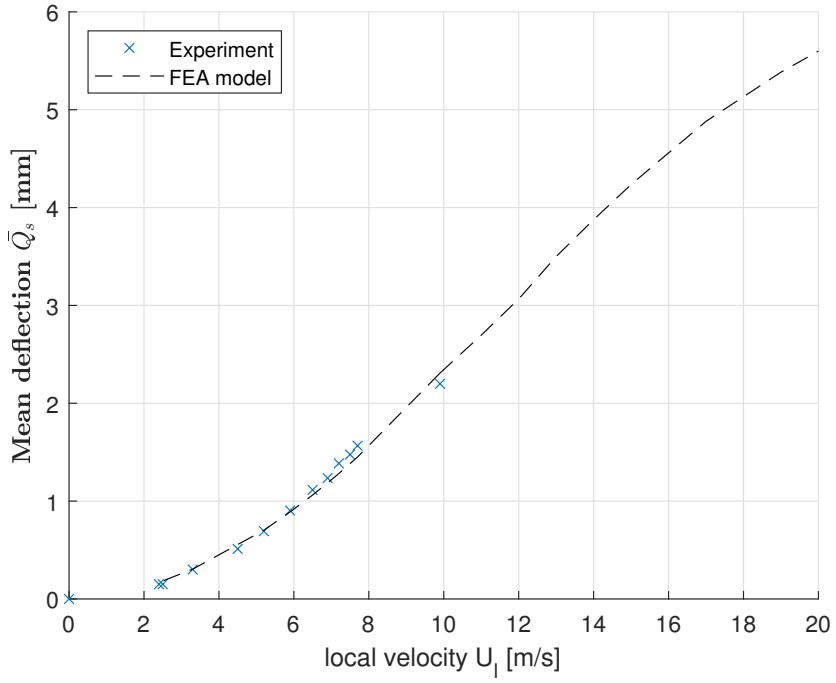

Figure 5. Tip deflection of pillar no. 1 measured against the results from the FEA simulation with variation in wall-jet velocity. Symbols: measurements with the wall-jet facility; dashed line: simulations.

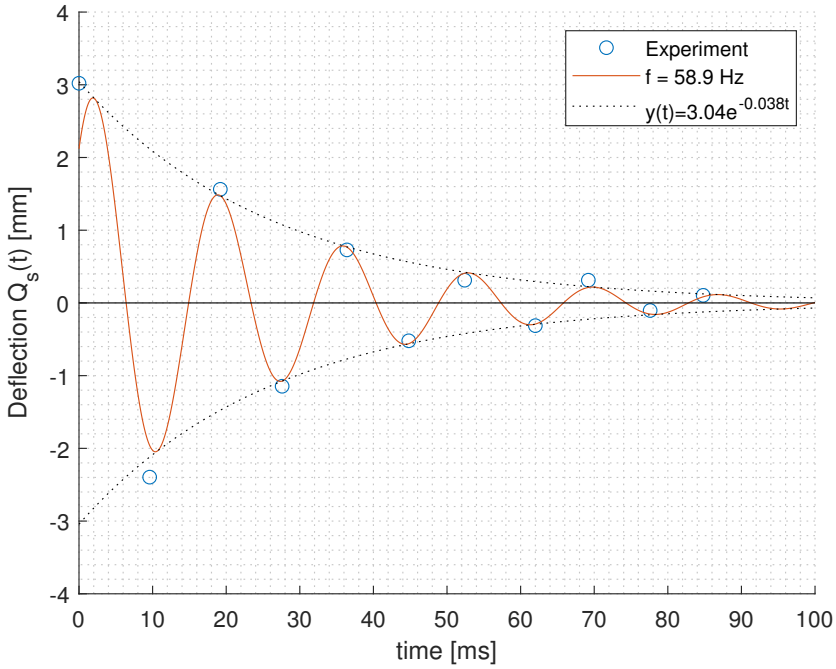

Figure 6. Response of the flexible pillar when released from forced bend to free relaxation back to its resting position. Symbols: measurements at the peak tip excursions; solid line: fit with a damped harmonic oscillation at natural frequency of 58.9 Hz; dashed line: fit to the amplitude-dampening function.

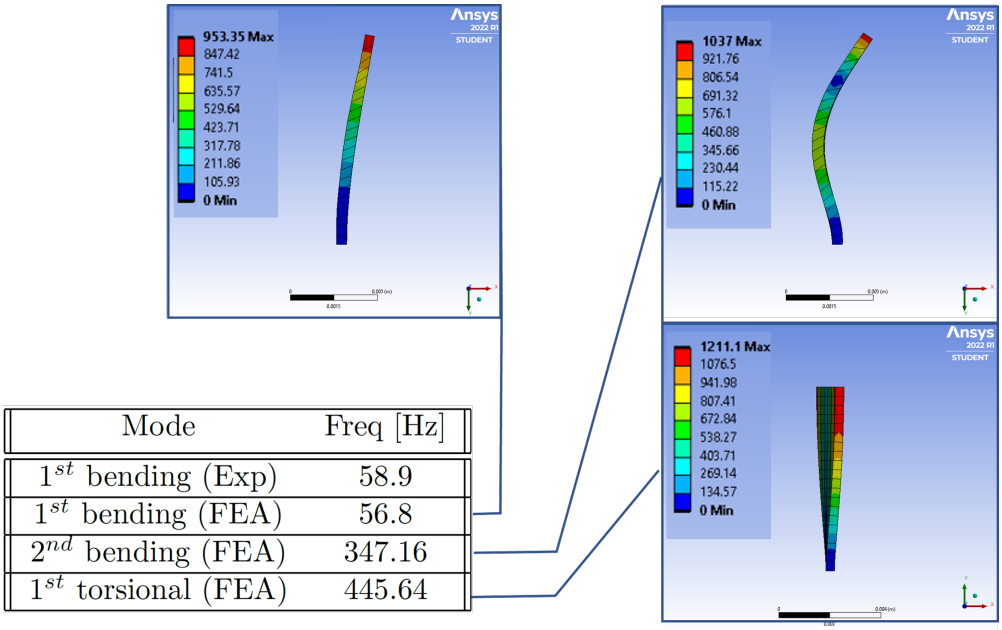

Mode	Freq [Hz]
1^{st} bending (Exp)	58.9
1^{st} bending (FEA)	56.8
2^{nd} bending (FEA)	347.16
1^{st} torsional (FEA)	445.64

Figure 7. Structural modes of the sensor and corresponding onset frequencies.

3.2. Aerofoil Experiment

The wind tunnel experiments with the prepared aerofoil were carried out at varying AoA and at a free-stream velocity of 15 m/s, corresponding to a Reynolds number of 200,000. Pillar motion tracking was carried out at a sampling rate of 500 Hz.

The time series of tip deflections $Q(t)$ for pillars 1 to 6 (leading edge to trailing edge) were output and post-processed as outlined above. The mean deflection of the pillars $\overline{Q}$ alone was first considered for varying AoA. First, the mean deflection of the first pillar $\overline{Q_1}$ is seen to be largely unaffected by changes of AoA until separation, as changes in boundary layer thickness and profile have a negligible effect on the mean tip deflection of that pillar, lying nearer to the leading edge. Furthermore, the deflection of the pillar is already fairly large and close to the reconfiguration limit observed in (Figure 5). There is an overall increase in deflection observed in the leading-most pillar between zero lift and the lifting conditions visible in (Figure 8a), which is expected due to the flow acceleration; however, it is not concurrent in further pre-stall increases in the angle of attack. It is possible that this decrease in sensitivity is due to the reconfiguration limit. Additionally, as the AoA changes, so do the boundary layer chord-wise growth rate and profile, which have an effect on the mean bending of the pillars $\overline{Q}$. The effects of boundary layer changes on the deflection of flexible pillar structures have previously been investigated [7]; they are seen herein for the first data points of (Figure 8a) and are illustrated more clearly in (Figure 8b). The relative tip deflection for pillars aft of the second pillar to the first pillar, $\overline{Q_{s,N}} - \overline{Q_{s,1}}$, is therefore seen to increase as the AoA increases while approaching stall. This allowed for a measure of instantaneous AoA by observing this relative deflection. Seeing that the deflection of the first pillar is relatively unaffected by changes in AoA, while later pillars are clearly affected, allows for there to be an expected unique combination of the total deflection of the leading-edge-most pillar and the relative deflection of aft pillars, thus providing a reading of instantaneous free-stream velocity and AoA, given the clear sensitivity of the leading-edge pillar to the changes in free-stream velocity, as seen in (Figure 5), and its insensitivity to changes in AoA, as shown in (Figure 8b).

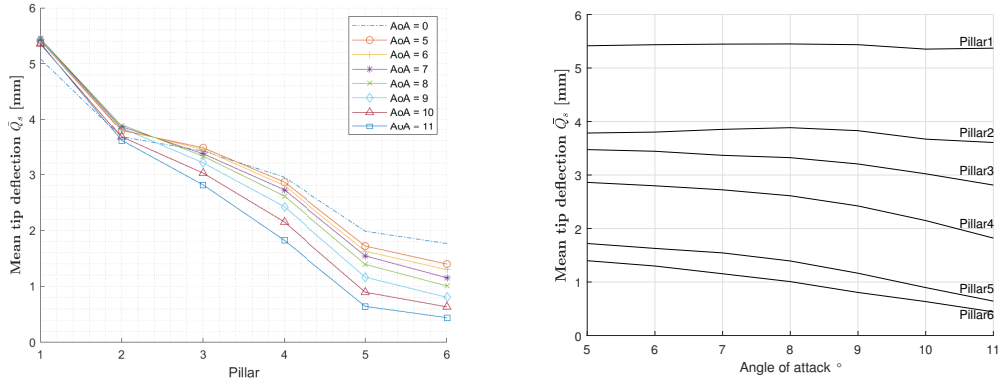

(**a**) (**b**)

Figure 8. Mean tip deflection $\overline{Q}$ at different sensor positions along the chord (**a**) and for varying AoA (**b**).

Moreover, it can be seen in (Figure 9) that the range of fluctuations within a 99% confidence interval becomes larger with chord-wise distance, eventually moving into negative deflections, which occur more frequently at critical AoAs immediate to stall. Figure 10 shows how reversed (negative) deflections begin to reliably appear within the filtered data within the 1.5 interquartile range, in addition to stronger negative deflections outside this range. This is due to the reversed flow affecting the pillar and is the footprint of growing instabilities in the flow.

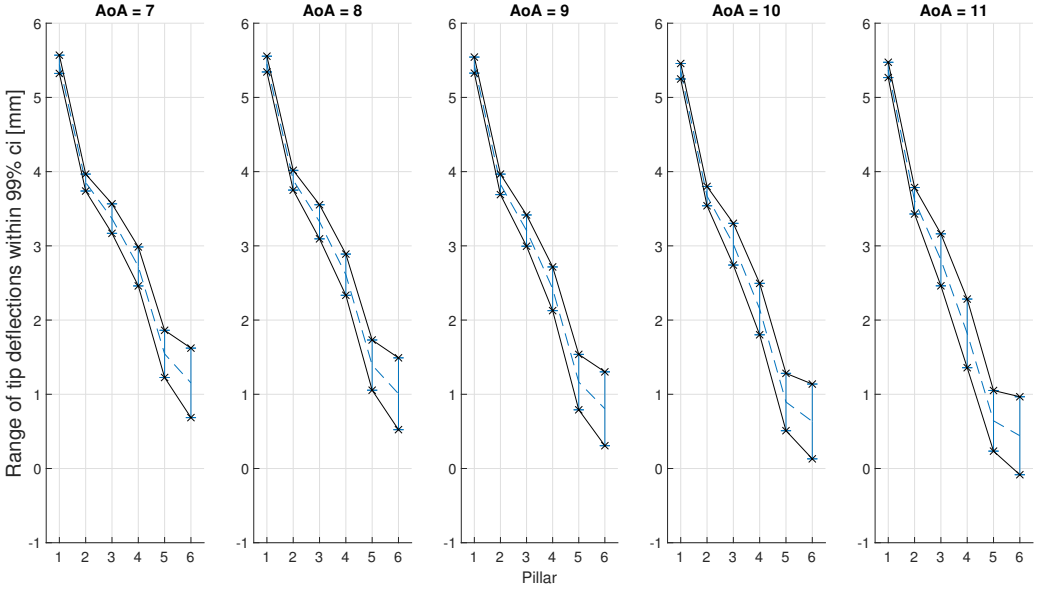

Figure 9. Mean deflection (dashed blue line) and range of fluctuations within 99% confidence interval (solid black lines) for each pillar for moderate, pre-stall AoA. The fluctuation range data points are represented by asterisks.

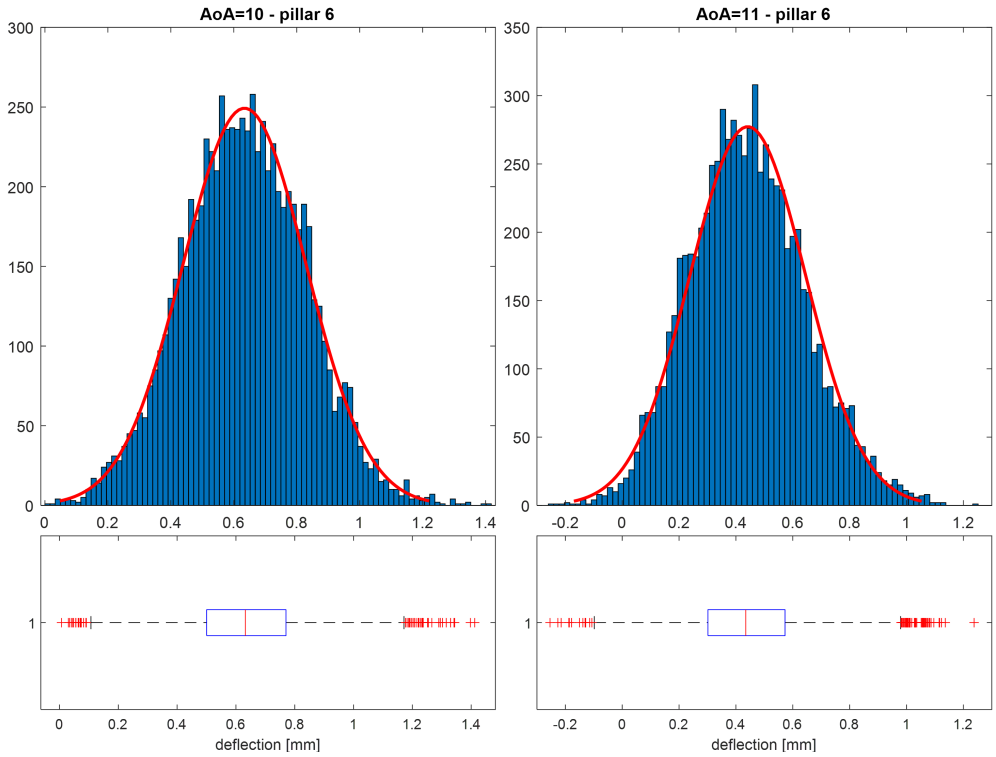

Figure 10. Histogram with superimposed Gaussian fit and box-plot of median and interquartile range of aft-most pillar deflections at pre-stall AoA 10° (**left**) and 11° (**right**) for sample sizes of 7500 samples recorded at a sample rate of 500 fps (whiskers on box-plot represent 1.5*IQR).

Figure 11 shows the results for an exemplary pillar at 45% chord from a spectral analysis of the displacement values. This was carried out with the low-pass filtered time series of pillar tip deflections to exclude peaks from oscillations of the pillars' natural frequency. The results for an AoA of 0° and 7° are included. These show no discernible peaks of notable strength. Low-frequency oscillations start to be detected by this pillar at an AoA of 8°, with a relatively weak peak beginning to form at St = 0.016. With further increases in AoA, a dominant oscillation frequency emerges, whose Strouhal numbers (defined as fc/u) increase up to 0.027 with the increase in incidence to critical pre-stall angles, in agreement with the findings of [14]. Therefore, the peak is hypothesised to be linked to quasi-periodic shear-layer flapping downstream of the laminar separation bubble.

What is noticed is that not only does the peak frequency increase with increases in AoA, but also, the peak strength increases markedly as the wing approaches stall. These are both quantities that can act as markers for instantaneous AoA sensing and indicators for incipient separation and stall. The Strouhal number of the most dominant oscillations for the AoA shows the trend for those pre-stall AoA where the low-frequency oscillations appear (Figure 11). These lie within the range of the low-frequency oscillations observed by [14,15].

To investigate the validity of such markers for dynamic motions of the aerofoil, thus also indicating early incipient stall, tests were run for ramp-up motion experiments with the aerofoil. In such a run, the AoA of the model was steadily changed from 0 to 15 degrees at a rate of (1.85 degrees/s), corresponding to a reduced frequency $k = 0.5 \times 10^{-3}$.

$$k = \frac{\rho \times f \times c}{U_{inf}} \tag{4}$$

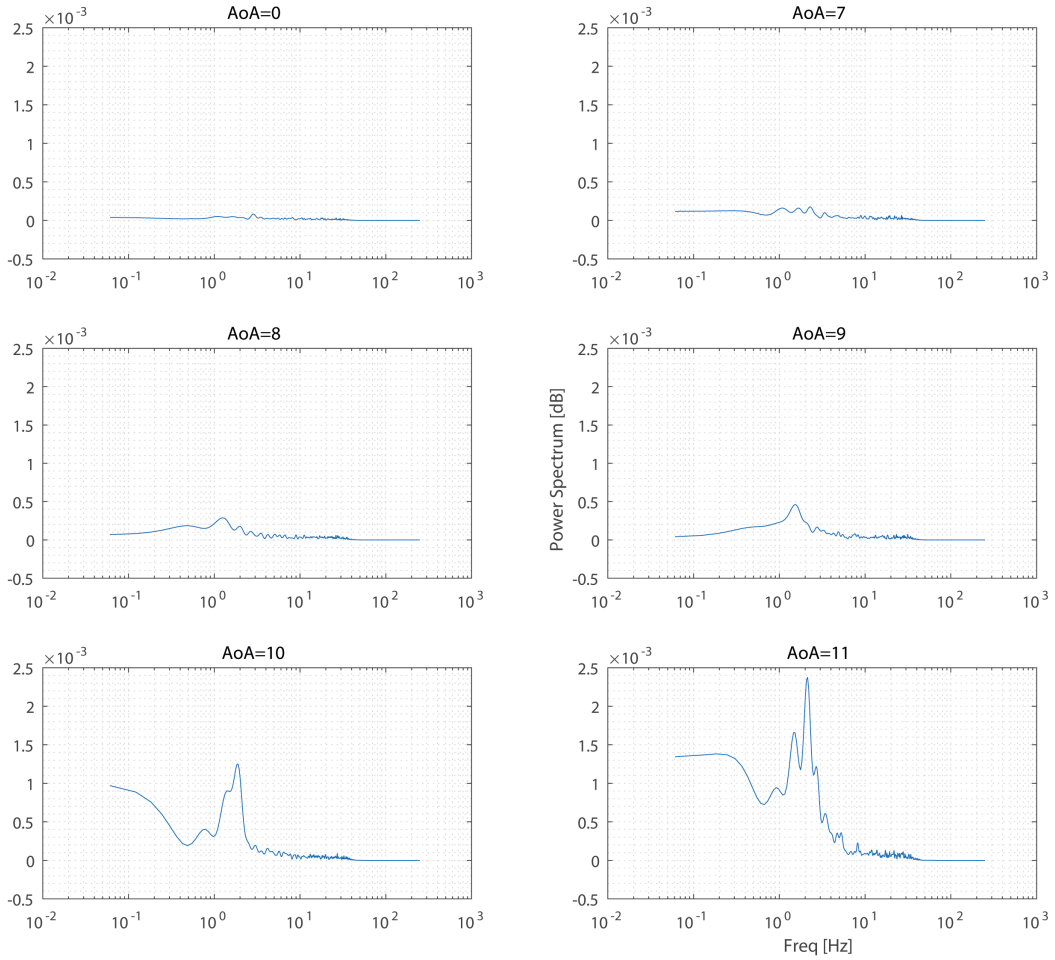

Figure 11. Spectral analysis of pillar deflections at increasing AoA showing the increase in frequency and intensity of the low-frequency oscillations as stall is approached. The peaks for AoAs of 8, 9, 10, and 11 correspond to Strouhal numbers of 0.016, 0.019, 0.024, and 0.027, respectively

Figure 12 shows the original data and the results after low-pass filtering for each pillar. As the aerofoil approaches separation (approx. 5–6 s or 9–11°), similar low-frequency oscillations to those in the steady aerofoil situation at higher AoA become pronounced. Therefore, it is concluded that the detection of specific low-frequency oscillations in the above-discussed Strouhal number range is unique to incipient separation.

Separation is characterised by a complete reversal of a pillar, followed by an oscillation about the 0 position. This is explained by the separated flow structures over the suction side of the aerofoil and can be seen visualised in Figures 12 and 13, where post-separation, the signals return to a zero or near-zero mean with more stochastic oscillations of higher RMS. This is akin to reversing tufts in a tuft-visualisation experiment. A ramp-up tuft visualisation experiment was carried out with simultaneous pillars to contrast this characteristic reversal to the more commonly used reversing tufts and is shown below in (Figure 14). The separated flow visualisation shown in (Figure 13) was obtained at a chord-wise Reynolds number of 70×10^3, which allowed for conditions facilitating improved flow-visualisation quality. This allowed for a visualisation of the sensor interaction with stalled flow to shed light on the subsequent results.

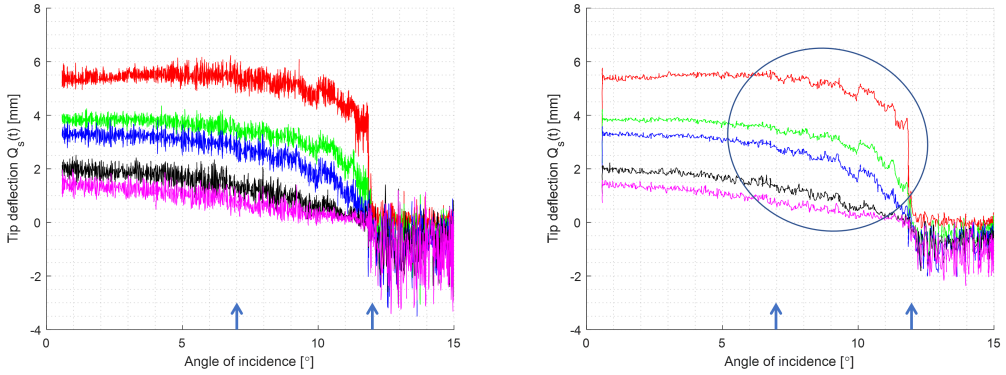

(**a**) (**b**)

Figure 12. Results from ramp-up study showing oscillation and pre-stall behaviour of pillar tip deflections. The low-frequency oscillations appear at pre-stall angles on the unfiltered results (**a**), and are more apparent after low-pass filtering (**b**) where they are encircled in blue and the angles demarcated with blue arrows. Pillars no. 1 to 5 shown in red, green, blue, black, and magenta, respectively.

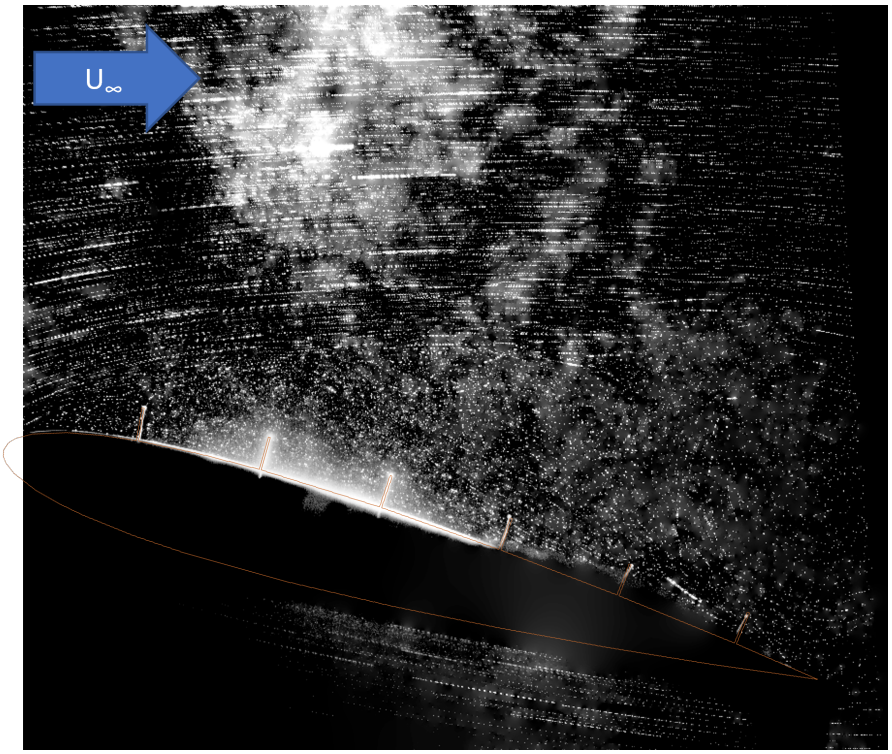

Figure 13. A flow visualisation image illustrating the post-stall flow interaction with the pillars. Flow is from left to right; pillars are on suction side. Image blended from frames of post-stall flow visualisation tests carried out at a post-stall $AoA = 16°$ and a chord Reynolds number of 70×10^3.

Additional flow field measurements were made using high-speed particle image velocimetry to further investigate the low-frequency oscillations. A virtual probe was put at a chord of 45% and 3 mm wall distance to analyse the fluctuations in the streamwise velocity component. Figure 15 shows the probe signal in the PIV results compared to the smoothed and filtered results from the third pillar from both the high-speed recordings and the object tracking camera recordings. The object tracking camera was trained on the central pillars to track tip deflections with a sampling rate of 250 Hz. The comparison of all three plots show striking similarity of low-frequency oscillations, although the signals were not taken simultaneously.

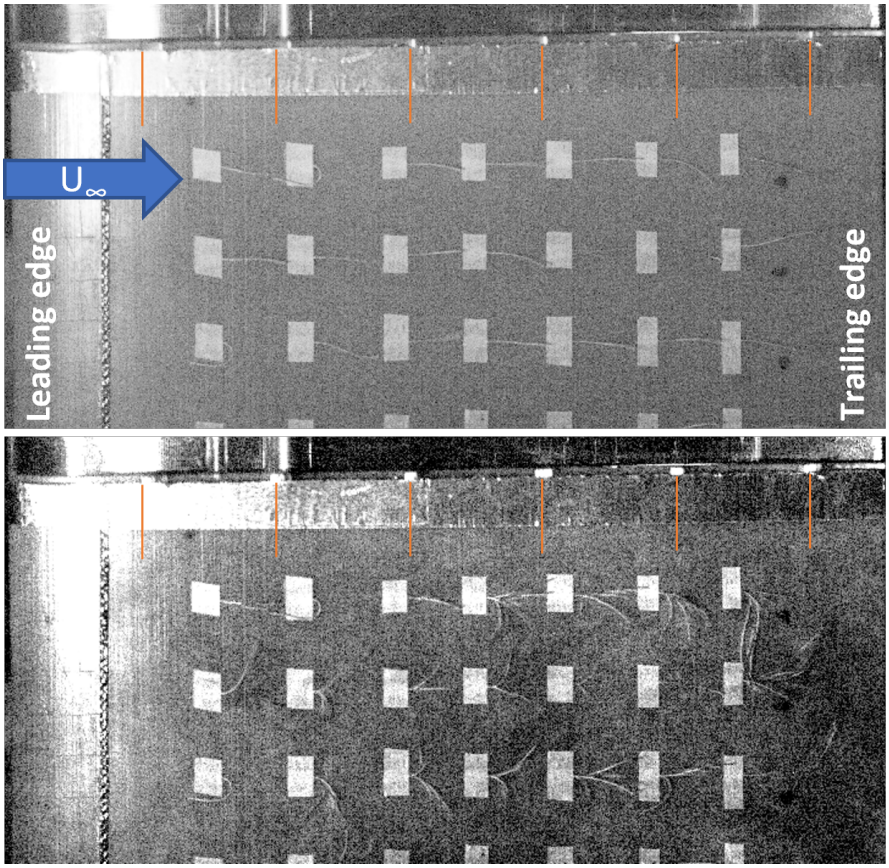

Figure 14. (**Top**) Attached (pre-stall) flow over the aerofoil showing full positive deflections on all pillars. (**Bottom**) A multi-exposed image of 15 frames showing the pillar behaviour during post-stall separation. Flow in both images is left to right, and the orange markers mark the wind-off position of each sensor.

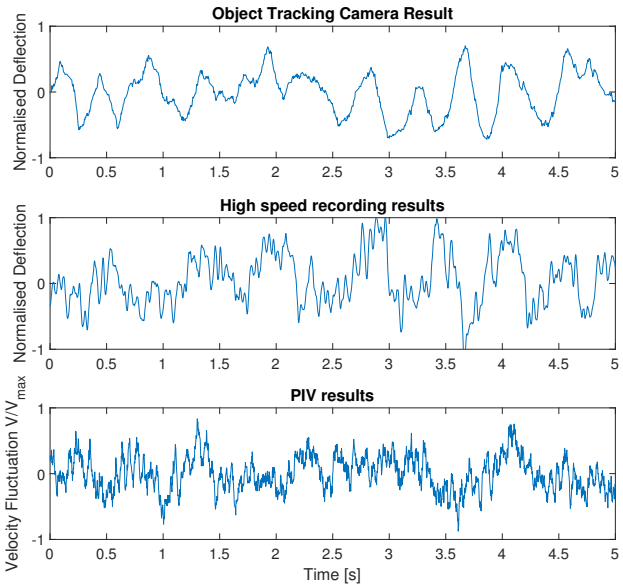

Figure 15. Fluctuating component of deflection relative to the mean from the pillar 3 (at 45% chord) are shown from 3 separate experiments, normalised with the maximum. (**top**) Results from the object tracking camera, (**centre**) from the processed images of the high-speed recording, and (**bottom**) from the streamwise velocity component at the probe location from the time-resolved PIV recordings, all at an AoA of 10 degrees.

4. Discussion

The experimental work presented in this paper has shown the potential for optically tracked flexible pillar sensors to act as "digital tufts", providing real-time high temporal resolution data that correlate with local flow velocities, from which further data of the flow structures over the wing can be summarized. The use of these sensors for aerofoil sensing was tested, and particular markers were identified that characterized incipient stall conditions. These markers include negative deflections of the aft-most pillars, an increase in the RMS of the fluctuations from the aft-most pillars, and low-frequency oscillations in the fluctuating component of sensor deflection.

For static conditions of the aerofoil, the time-averaged deflections of all pillars across the chord of the wing show a unique combination that is indicative of the instantaneous AoA prior to stall. That is, by observation of the trend of mean deflection of the sensors in downstream direction, which is represented by the gradient of the mean pillar deflections, it can be seen as unique to each AoA. This result is due to the variation of the boundary layer with chord and AoA (Figure 16) and the resulting integration effect on the pillar sensors. The sensitivity of such a type of sensor to the thickness and the shape factor of the boundary layer has been shown already in [7] and is confirmed herein by the observed results for varying AoA.

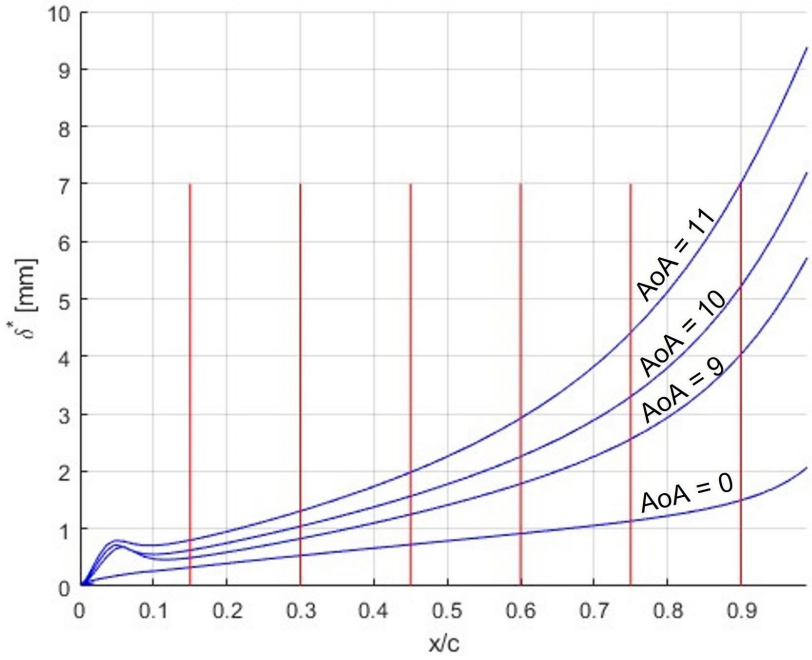

Figure 16. Estimation of the displacement thickness as the AoA approaches stall, with reference to pillar position and length overlaid in red. Values of δ^* were obtained using xfoil [24].

This use case is intended as a proof of concept for this type sensors to investigate their capability of sensing aerofoil flow conditions and detecting incipient stall. It was seen that particular markers were present to characterise those conditions. Firstly, instances of negative deflection, that is, the deflection of the pillar sensors in the direction opposite to the free-stream flow and past the wind-off position, were seen on the aft-most pillars. These are indicative of growing local flow instabilities and reversed flow situations, which were seen to be present in the high pre-stall AoAs. Moreover, by monitoring the fluctuating component of sensor deflection, an increase in the RMS of the fluctuations from those aft-most pillars was also seen in those AoAs incipient to flow separation and stall. Both of these markers occur with a response time in the order of the sensor response time, which is less than 100 ms. Finally, spectral analysis of the fluctating components from the signal showed particular low-frequency oscillations occurring in the AoAs leading up to stall. Previous data in literature let us hypothesise that the low-frequency oscillations are linked

to the quasi-periodic breathing of the laminar separation bubble formed over the suction side of the wing. The frequency and intensity of such a signature, as tracked by the flexible pillar sensors, can be correlated with the flight condition, specifically the AoA. Alternatively, other correlations can be tested for specific flight conditions in training or learned from application to be identified by training a specialised neural network. However the applications are not limited to aerofoil sensing, and further development would be required for direct application on commercial UAVs. Although the mean component is fairly robust and with a low response time, particularly when monitoring over an array where the redundancy of the received signals would allow for a reliable reading, the oscillations used to characterise incipient stall are of a relatively low frequency, occurring at Strouhal numbers on the order of 0.02. Thus, they would be marginally useful as a standalone system, but further work incorporating such sensors into a suite would allow such measurements to be used in conjunction with other measurements, such as a sharp increase in the detected angle of incidence, to more reliably characterise incipient stall.

Optical tracking was explored herein as a method to obtain the pillar deflection readings remotely without any physical connection to the sensor. This is meant to exploit the physical nature of the sensor deflections, which would not be present with other measurement types, such as pressure measurements. The applications of the optical tracking of flow measurements would be where physical connections are not possible or not optimal, and such lightweight optical equipment may offer an alternative to obtain measurements from areas that would otherwise either go unsensed or where it would mitigate the cost justification for obtaining measurements from such an area. Furthermore, where pressure sensing may not be applicable, such as in underwater flows, optically tracked pillars can act as an alternative to provide a flow picture for analysis.

There is a general limitation with such hair-type sensor arrays. First is the fact that those sensors are invasive to the flow, and second is the fact that their dynamics may interfere with the output of one another; thus, the pillars must be spaced apart appropriately to avoid interaction effects and to ensure that the reading from each pillar is representative of the surrounding flow conditions. The pillars in the use cases presented herein were spaced at 20 diameters apart to mitigate inter-pillar disturbances. A further improvement would be to offset every other pillar in the span-wise direction to further lessen these effects. That way, their readings can be considered collectively, as in (Figure 8), or individually, as in (Figure 11), to provide accurate flow condition information. It is, furthermore, suggested in future designs to size the pillars that are unaffected by boundary layer flow appropriately so that they are sufficiently distant from the reconfiguration limit of deflection while maintaining sensitivity along the remainder of the array. This can be achieved by varying the leading-edge-most pillar dimensions and structural properties from those further aft. Moreover, the sensors presented herein are intended as a proof of concept rather than a plug-and-play solution. Further work is required in terms of manufacturing technology and equipment to produce pillars with dimensions that can vary depending on the operating fluid. The pillars were designed to find a balance between facilitating optical tracking from standard optical systems mounted on-board and providing the least possible disturbance to the flow. This is a trade-off between reducing the dimensions of the pillars such that their invasive character is reduced and the resolution limit of the imaging system, where smaller structures lead to less visibility and lower optical resolution. The arrangement used herein, together with the rather moderate Re-number flows tested, represent a good practical compromise of the given system for the envisioned application of such sensors on small UAVs.

Pillar sensors can provide a multitude of velocity and velocity-derived data to be used for real-time diagnostics. Compared to wool tuft visualisations, the pillar sensors' capability to encode the mean and fluctuating part of the local velocity provides more rich diagnostics of the current flow state. Spectral analyses of the signal in conjunction with pattern recognition algorithms were used here to identify specific quantities unique to the flight conditions. Introducing and training a specialised neural network to identify

the local flow conditions, such as was carried out with similar nature-inspired sensors in [19], is planned as a further development of this system. Furthermore, spatial near-wall flow field recovery techniques can be applied from the relative sparse sensor placement using deep learning. For timely decision making and response to signals in an aeronautical system in situ, the signals must be collected and processed "on the fly" with optical systems that can filter out irrelevant data using physical means such as wavelength separation, in addition to computational means, and then process that data within the required time period. Using on-line object tracking, it was possible to train the camera on the relevant pillar tips to instantaneously output a time-series of coordinates corresponding to the pillar tip deflections for a specified time period and sampling rate. These type of recordings with multiple levels of filtering and pre-processing are often affected by corrupt or sparse data. Emerging technologies in reconstructing such data structures such as sparse representation and compressive sensing can allow for the timely and efficient onboard processing of these data for subsequent flight or flow control decision making [25].

Finally, span-wise data can be obtained by including an entire array of these pillar sensors spanning a wing. These can be used over the skin of a wing in a wind tunnel or fitted onto the system in operation. An example application for such an array would be to characterise localised stall over the span of a washed-out wing, where stall typically occurs near the wing-root, providing a real-time reading of remaining aerodynamic lift or aileron efficiency. Current work on the sensors is looking at local flow conditions at post-stall AoA as a way of characterising span-wise local stall phenomena simply from tip-deflection data of the pillars (Figure 17). The response from the fore-most pillars in this paper were seen to be least affected by local flow instabilities and more reflective of the free-stream flow conditions. Thus, further work incorporating these pillars into 2D arrays will investigate the capability of obtaining a fuller picture of the free-stream flow by monitoring the response of those fore-most pillars to induced flow disturbances, such as wake-turbulence or gusts. Coherent signatures of flow events over several pillar sensor positions is a way to distinguish noise from relevant structures. Thus, these can be separated by eliminating those signals that occur with no chord-wise phase delays, and for further robustness, can be correlated with signals from an on-board accelerometer. This, coupled with the developed signal processing from the sensors, will allow the ability to provide diagnostic data for an aerodynamic system's performance over a wide regime of flow conditions. This leads into the development of a system of biologically inspired sensors, which react in a predictable manner to changes in flow conditions within the flight regime of small- to medium-sized UAVs, which can be used in situ to promptly provide diagnostic data to a flight control system or can be used for diagnostics in experimental conditions.

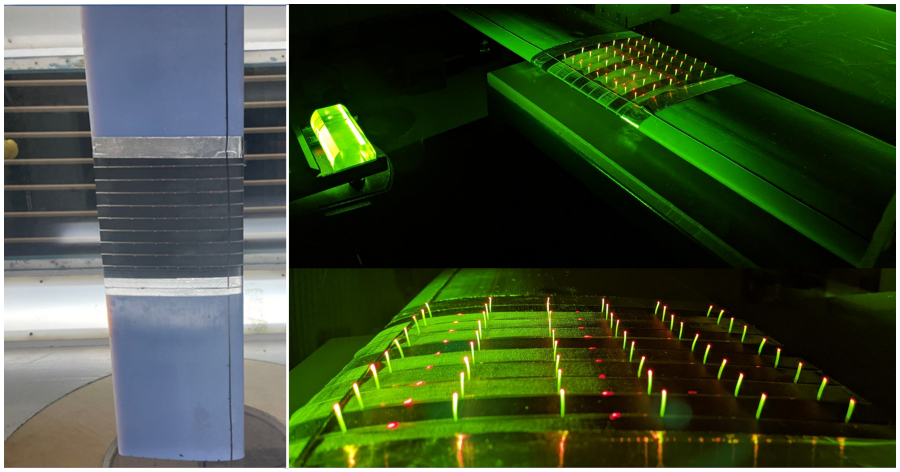

Figure 17. Setup of experiment with array of sensors attached. The tips are illuminated with green LED light.

5. Conclusions

This paper has presented the results of experimental work on optically tracked flexible pillar sensors and their application for aerofoil sensing. The results show that these sensors have the potential to act as "digital tufts", providing real-time high temporal resolution data that correlate with local flow velocities. The use case of these sensors in an aerofoil sensing capacity has shown their ability to provide information on particular markers that characterize pre-stall flow conditions, including negative deflections of the aft-most pillars, an increase in the RMS of the fluctuations from the aft-most pillars, and low-frequency oscillations in the fluctuating component of sensor deflection.

The optical tracking of sensor deflections allows remote measurement without any physical connection to the sensor, which could provide an alternative to obtaining measurements from areas that would otherwise be inaccessible. However, there are limitations to these hair-type sensor arrays, including the fact that they may be invasive to the flow at larger sizes and their dynamics may interfere with the output of one another if not sized and situated carefully. Future work should focus on improving the sensors' manufacturing process to produce pillars that are optimized for specific flow conditions and that can be integrated into a suite of measurements to provide accurate flow condition information.

Author Contributions: Conceptualization, O.S. and C.B.; methodology, software, and validation, O.S. and C.B.; formal analysis, investigation, visualization, and data curation O.S.; writing—original draft preparation, O.S.; writing—review and editing, O.S. and C.B.; supervision, project administration, resources, and funding acquisition, C.B. All authors have read and agreed to the published version of the manuscript.

Funding: The position of Omar Selim is funded by the George Daniels Educational Trust. The position of Professor Christoph Brücker is co-funded by BAE SYSTEMS and the Royal Academy of Engineering (Research Chair No. RCSRF1617/4/11).

Data Availability Statement: The data presented in this study are available on request from the corresponding author. The data are not publicly available at the time of publication due to their usage for the preparation of a successive publication on a further extension of our hypothesis.

Acknowledgments: The position of Omar Selim is funded by the George Daniels Educational Trust. The position of Christoph Brücker is co-funded by BAE SYSTEMS and the Royal Academy of Engineering (Research Chair No. RCSRF1617/4/11), all of whom are gratefully acknowledged. The authors would also like to acknowledge and express their gratitude to Deutsche Forschungsgemeinschaft (DFG) for their support with the provision of some of the optical systems used in this study. Additionally, the authors would like to express thanks to Alecsandra Court for her role in the continuation and development of the pillar sensor arrays and Ibrahim Kejje for his diligent work on the development of the calibration wind tunnel.

Conflicts of Interest: The authors declare no conflict of interest. The funders had no role in the design of the study; in the collection, analyses, or interpretation of data; in the writing of the manuscript; or in the decision to publish the results

References

1. Choi, S.Y.; Cha, D. Unmanned aerial vehicles using machine learning for autonomous flight; state-of-the-art. *Adv. Robot.* **2019**, *33*, 265–277. [CrossRef]
2. Blösch, M.; Weiss, S.; Scaramuzza, D.; Siegwart, R. Vision based MAV navigation in unknown and unstructured environments. In Proceedings of the 2010 IEEE International Conference on Robotics and Automation, Anchorage, AK, USA, 3–8 May 2010; pp. 21–28.
3. Mohamed, A.; Watkins, S.; Clothier, R.; Abdulrahim, M.; Massey, K.; Sabatini, R. Fixed-wing MAV attitude stability in atmospheric turbulence—Part 2: Investigating biologically-inspired sensors. *Prog. Aerosp. Sci.* **2014**, *71*, 1–13. [CrossRef]
4. Araujo-Estrada, S.A.; Windsor, S.P. Aerodynamic state and loads estimation using bioinspired distributed sensing. *J. Aircr.* **2021**, *58*, 704–716. [CrossRef]
5. Brücker, C.; Schlegel, D.; Triep, M. Feather vibration as a stimulus for sensing incipient separation in falcon diving flight. *Nat. Resour.* **2016**, *7*, 411–422. [CrossRef]
6. Selim, O.; Gowree, E.R.; Lagemann, C.; Talboys, E.; Jagadeesh, C.; Brücker, C. Peregrine Falcon's Dive: Pullout Maneuver and Flight Control Through Wing Morphing. *AIAA J.* **2021**, *59*, 3979–3987. [CrossRef]

7. Dickinson, B.T. Hair receptor sensitivity to changes in laminar boundary layer shape. *Bioinspir. Biomimetics* **2010**, *5*, 016002. [CrossRef] [PubMed]
8. Brücker, C.; Bauer, D.; Chaves, H. Dynamic response of micro-pillar sensors measuring fluctuating wall-shear-stress. *Exp. Fluids* **2007**, *42*, 737–749. [CrossRef]
9. Brücker, C. Evidence of rare backflow and skin-friction critical points in near-wall turbulence using micropillar imaging. *Phys. Fluids* **2015**, *27*, 031705. [CrossRef]
10. Counsil, J.N.; Goni Boulama, K. Low-reynolds-number aerodynamic performances of the NACA 0012 and Selig–Donovan 7003 Airfoils. *J. Aircr.* **2013**, *50*, 204–216. [CrossRef]
11. Kim, D.H.; Chang, J.W.; Chung, J. Low-Reynolds-number effect on aerodynamic characteristics of a NACA 0012 airfoil. *J. Aircr.* **2011**, *48*, 1212–1215. [CrossRef]
12. Winslow, J.; Otsuka, H.; Govindarajan, B.; Chopra, I. Basic understanding of airfoil characteristics at low Reynolds numbers (104–105). *J. Aircr.* **2018**, *55*, 1050–1061. [CrossRef]
13. Zaman, K.; McKinzie, D.; Rumsey, C. A natural low-frequency oscillation of the flow over an airfoil near stalling conditions. *J. Fluid Mech.* **1989**, *202*, 403–442. [CrossRef]
14. Tanaka, H. Flow visualization and PIV measurements of laminar separation bubble oscillating at low frequency on an airfoil near stall. In Proceedings of the 24th International Congress of the Aeronautical Sciences, Yokohama, Japan, 29 August–3 September 2004; pp. 1–15.
15. ElAwad, Y.A.; ElJack, E.M. Numerical investigation of the low-frequency flow oscillation over a NACA-0012 aerofoil at the inception of stall. *Int. J. Micro Air Veh.* **2019**, *11*, 1756829319833687. [CrossRef]
16. Selim, O.; Bruecker, C. Detecting separation pre-cursors using on-board optical tracking of flexible pillar sensors. In Proceedings of the 20th International Symposium on the Application of Laser and Imaging Techniques to Fluid Mechanics, Lisbon, Portugal, 11–14 July 2022; pp. 1162–1178.
17. Li, Q.; Stavropoulos-Vasilakis, E.; Koukouvinis, P.; Gavaises, M.; Bruecker, C.H. Micro-pillar sensor based wall-shear mapping in pulsating flows: In-situ calibration and measurements in an aortic heart-valve tester. *J. Fluids Struct.* **2021**, *105*, 103346. [CrossRef]
18. Raffel, M.; Willert, C.E.; Scarano, F.; Kähler, C.J.; Wereley, S.T.; Kompenhans, J. *Particle Image Velocimetry: A Practical Guide*; Springer: Berlin/Heidelberg, Germany, 1998; Volume 2.
19. Elshalakani, M.; Muthuramalingam, M.; Bruecker, C. A deep-learning model for underwater position sensing of a wake's source using artificial seal whiskers. *Sensors* **2020**, *20*, 3522. [CrossRef] [PubMed]
20. Oertel, H. *Prandtl's Essentials of Fluid Mechanics*; Springer: Berlin/Heidelberg, Germany, 2004.
21. Gosselin, F.P.; De Langre, E. Drag reduction by reconfiguration of a poroelastic system. *J. Fluids Struct.* **2011**, *27*, 1111–1123. [CrossRef]
22. Zheng, X.; Yu-Bin, L.; Pu, C.; Feng, S.; ZHANG, S.J.; Xiang-Rong, F. Flutter frequency based on bending-torsion coupling theory. In Proceedings of the 8th International Conference on Computational Methods (ICCM2017), Guilin, China, 25–29 July 2017.
23. Leclercq, T.; de Langre, E. Vortex-induced vibrations of cylinders bent by the flow. *J. Fluids Struct.* **2018**, *80*, 77–93. [CrossRef]
24. Drela, M. XFOIL: An analysis and design system for low Reynolds number airfoils. In *Low Reynolds Number Aerodynamics*; Springer: Berlin/Heidelberg, Germany, 1989; pp. 1–12.
25. Callaham, J.L.; Maeda, K.; Brunton, S.L. Robust flow reconstruction from limited measurements via sparse representation. *Phys. Rev. Fluids* **2019**, *4*, 103907. [CrossRef]